

Gravitational Redshifts of Clusters and Voids

Daiki Sakuma, Ayumu Terukina, and Kazuhiro Yamamoto
*Graduate School of Science, Department of Physics, Hiroshima University,
 Higashi-Hiroshima, Kagamiyama 1-3-1, 739-8526, Japan*

Chiaki Hikage

*Kavli Institute for the Physics and Mathematics of the Universe (Kavli IPMU, WPI),
 The University of Tokyo, 5-1-5 Kashiwanoha, Kashiwa, Chiba, 277-8583, Japan*

We investigate gravitational redshifts (signals of gravitational potential) in measurements of the redshifts of cosmological objects, i.e., central and satellite galaxies in clusters of galaxies, intracluster gas, as well as galaxies associated with voids by developing simple theoretical models. In the analysis with satellite galaxies in clusters, we develop a very simple analytic model for satellite galaxies virialised in halos, which enables us to evaluate the signals depending on the properties of the halo occupation distribution of galaxies. We obtain results consistent with recent previous results, though our results are restricted to the satellite galaxies inside the virial radius. In the analysis of intracluster gas, we develop a simple analytic model including the effect of random motions of gases, which are assumed to generate nonthermal pressure. We demonstrate a possible contribution of the random motions of gases to gravitational potential measurements. We also investigate a possible signature of the gravitational potential in measurements of galaxies associated with voids by utilizing a simple analytic model. We show that the second-order Hubble term, which appears in the expansion of the scale factor around the centre of a void, may make a significant contribution depending on the way the galaxy samples are analysed. The studies on the possible signals of gravitational potential for intracluster gases and voids are performed for the first time.

I. INTRODUCTION

Relativistic effects in the cosmological large-scale structure have been investigated by many authors [1–8]. Measurements of the gravitational redshifts^{#1} as a relativistic effect in measurements of the redshifts of cosmological objects, have been reported recently using galaxies associated with clusters [9, 10, 12]. Wojtak et al. first reported the detection of the gravitational redshift of satellite galaxies in and around clusters [9]. Zhao et al. pointed out the contribution of the transverse Doppler velocity of galaxies to measurements of the gravitational potential [10]. They also stressed the importance of the gravitational redshift as a test of general relativity and modified gravity models. Kaiser has pointed out that the nontrivial feature of the phase space distribution function of objects defined on the lightcone coordinate leads to an additional second-order Doppler term [11]. Furthermore, other relevant effects in the measurements of the gravitational potential of galaxies in clusters have been discussed [12, 13]. Thus, gravitational redshift is a unique tool for testing the general relativity and modified gravity theories.

Motivated by these recent works, we investigate possible signatures of the gravitational redshift in clusters of galaxies and voids. We consider three systems. The first consists of satellite galaxies virialised in halos of galaxy clusters, for which we derive a simple formula for the gravitational redshift with the use of the halo occupation distribution (HOD) description with central galaxies and satellite galaxies. Our investigation is different from the previous works in the following point: Our analysis is restricted to scales within the virial radius of a halo, but our simple analytic model is useful for understanding how the measurement of gravitational redshift depends on the HOD properties of galaxy samples. The second system concerns the gravitational redshift in observations of intracluster gas, which is motivated by the recent precise measurement of intracluster gas motions in the Perseus Cluster reported in Ref. [14]. A possible signature of the gravitational redshift in measurements of intracluster gas is investigated. In this analysis, we include the effect of random motions of the gas that explain the nonthermal pressure predicted by numerical simulations. Possible contamination of random motions of gases to a measurement of gravitation potential is pointed out for the first time. The third system comprises galaxies associated with voids. Because some galaxies might be found inside voids, we may consider the possibility of measuring the gravitational potential of voids. We investigate a possible signature of the gravitational potential of galaxies associated with voids. We stress that such an investigation is performed for the first time as far as we know.

^{#1} We use the terminology, *gravitational redshift*, to express the redshift including the signal of gravitational potential dominantly, although such signals are contaminated by the second order Doppler velocities and other higher order effects of the general relativity.

This paper is organised as follows. In Sec. II, we rederive a formula for the gravitational redshift given by Kaiser [11], starting from the geodesic equation. In Sec. III, we investigate the gravitational redshift in galaxy samples in redshift surveys, using the halo approach with the HOD with central galaxies and satellite galaxies. In Sec. IV, we demonstrate a possible signature of the gravitational redshift in measurements of intracluster gas. In Sec. V, we investigate a possible signature of the gravitational redshift of galaxies associated with voids. We also show that the contribution from a second-order Hubble term, which appears in the expansion of the scale factor around the centre of a void, can be significant depending on the range of projecting galaxies in the line-of-sight direction in the analysis. Section VI is devoted to a summary and conclusions. In the Appendix, we summarise our theoretical modelling for the clusters of galaxies in Sec. IV.

II. FORMULATION

Detection of the gravitational redshift of galaxies in and near clusters of galaxies has been reported in Refs. [9, 10, 12]. The theoretical formula developed by Kaiser is practical and useful [11, 13]; we rederive it, starting from the geodesic equation for a photon. We focus on the gravitational redshift in a system comprising a cluster of galaxies and voids, which are structures of much smaller than the horizon scale. Therefore, the Newtonian gauge is useful and efficient; its line element is written as

$$ds^2 = a(\eta)^2[-(1 + 2\psi)d\eta^2 + (1 + 2\phi)d\mathbf{x}^2], \quad (1)$$

where $a(\eta)$ is the scale factor as a function of the conformal time η , and ψ and ϕ are the gravitational potential and the curvature potential, respectively. Up to the first order of ψ and ϕ , the geodesic equation for a photon leads to (see, e.g., [15])

$$\frac{1}{p} \frac{dp}{d\eta} = -\mathcal{H} - \frac{\partial\phi}{\partial\eta} - \hat{p}^i \frac{\partial\psi}{\partial x^i}, \quad (2)$$

where p is the physical energy of the photon (equivalent to the physical momentum in units of $c = 1$) in the cosmological rest frame, \hat{p}^i is the unit vector of the photon momentum satisfying $\delta_{ij}\hat{p}^i\hat{p}^j = 1$, we defined $\mathcal{H} = a'/a$, and the prime denotes differentiation with respect to the conformal time η .

Using the relations

$$\frac{d\psi(\eta, \mathbf{x}^i(\eta))}{d\eta} = \frac{\partial\psi}{\partial\eta} + \frac{dx^i}{d\eta} \frac{\partial\psi}{\partial x^i}, \quad (3)$$

$$\frac{dx^i}{d\eta} = \hat{p}^i(1 + \psi - \phi), \quad (4)$$

and integrating from η_j to η_0 , where η_j is the conformal time when the photon is emitted from the j th object and we observe it at the present time η_0 , we find that Eq. (2) yields the following solution up to the first order of ϕ and ψ :

$$\frac{p(\eta_0)}{p(\eta_j)} = \frac{a(\eta_j)}{a(\eta_0)} \exp \left\{ - \int_{\eta_j}^{\eta_0} (\phi'(\eta, \mathbf{x}(\eta)) - \psi'(\eta, \mathbf{x}(\eta))) d\eta - \psi(\eta_0, \mathbf{x}(\eta_0)) + \psi(\eta_j, \mathbf{x}(\eta_j)) \right\}, \quad (5)$$

where $\mathbf{x}(\eta_j)$ is the position of the j th object at the emission of the photon (see Fig. 1). Hereafter, we assume $a(\eta_0) = 1$. When the j th object has the peculiar velocity \mathbf{v}_j , the observational redshift is multiplied by the factor $(1 + \boldsymbol{\gamma} \cdot \mathbf{v}_j) / \sqrt{1 - \mathbf{v}_j^2}$, where $\boldsymbol{\gamma}$ is the unit vector of the line-of-sight direction. Then, the redshift of the j th object is given by

$$1 + z_j = \frac{1}{a(\eta_j)} \exp \left\{ \int_{\eta_j}^{\eta_0} (\phi' - \psi') d\eta + \psi(\eta_0, \mathbf{x}(\eta_0)) - \psi(\eta_j, \mathbf{x}(\eta_j)) \right\} \frac{1 + \boldsymbol{\gamma} \cdot \mathbf{v}_j}{\sqrt{1 - \mathbf{v}_j^2}}. \quad (6)$$

We rewrite the expression on the right-hand-side of Eq. (6) as follows. First, assuming nonrelativistic motion ($|\mathbf{v}| \ll 1$), we may write

$$\frac{1 + \boldsymbol{\gamma} \cdot \mathbf{v}_j}{\sqrt{1 - \mathbf{v}_j^2}} \simeq 1 + \boldsymbol{\gamma} \cdot \mathbf{v}_j + \frac{1}{2} \mathbf{v}_j^2. \quad (7)$$

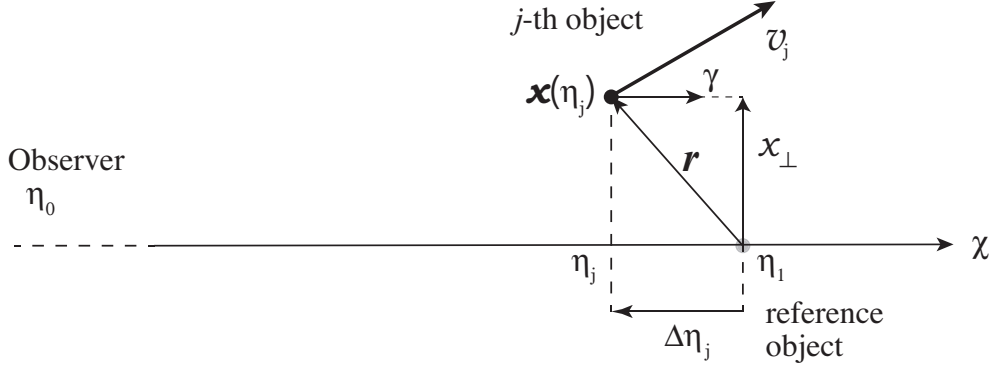


FIG. 1: Variables and coordinates. γ is the unit vector of the line-of-sight direction, and we also define $\chi = \eta_0 - \eta_1$.

Here we call the terms $\gamma \cdot \mathbf{v}_j$ and $\frac{1}{2}\mathbf{v}_j^2$ the first-order Doppler term and the second-order Doppler term, respectively. Up to the first order of metric perturbations, we also write

$$\begin{aligned} & \exp \left\{ \int_{\eta_j}^{\eta_0} (\phi' - \psi') d\eta + \psi(\eta_0, \mathbf{x}(\eta_0)) - \psi(\eta_j, \mathbf{x}(\eta_j)) \right\} \\ & \simeq 1 + \int_{\eta_j}^{\eta_0} (\phi' - \psi') d\eta + \psi(\eta_0, \mathbf{x}(\eta_0)) - \psi(\eta_j, \mathbf{x}(\eta_j)). \end{aligned} \quad (8)$$

In this expression, we call the term $\int_{\eta_j}^{\eta_0} (\phi' - \psi') d\eta$ the integrated Sachs–Wolfe term. $\psi(\eta_0, \mathbf{x}(\eta_0))$ and $\psi(\eta_j, \mathbf{x}(\eta_j))$ represent the gravitational potential of the observer and that of the j th object, respectively.

Furthermore, by introducing the time η_1 and setting $\eta_j = \eta_1 + \Delta\eta_j$ (see Fig. 1), we expand $1/a(\eta_j)$ as

$$\frac{1}{a(\eta_j)} \simeq \frac{1}{a(\eta_1)} \left\{ 1 - \mathcal{H}(\eta_1)\Delta\eta_j + \left(\mathcal{H}^2(\eta_1) - \frac{1}{2} \frac{a''(\eta_1)}{a(\eta_1)} \right) \Delta\eta_j^2 + \mathcal{O}(\Delta\eta_j^3) \right\}. \quad (9)$$

In this expansion, as shown in Fig. 1, we assume that a photon is emitted from the object located at the position specified by the comoving distance $\chi = \eta_0 - \eta_1$ and $\mathbf{x}_\perp = 0$ at the conformal time η_1 and that the observer receives the photon at the time η_0 , where we suppose that the position is the centre of a cluster or a void. We call this object the *reference object*. In Eq. (9), we call the terms $-\mathcal{H}(\eta_1)\Delta\eta_j$ and $(\mathcal{H}^2(\eta_1) - a''(\eta_1)/2a(\eta_1))\Delta\eta_j^2$ the first-order Hubble term and the second-order Hubble term, respectively.

Combining the above results, we have

$$\begin{aligned} 1 + z_j & \simeq (1 + z_1) \left\{ 1 - \mathcal{H}(\eta_1)\Delta\eta_j + \left(\mathcal{H}^2(\eta_1) - \frac{1}{2} \frac{a''(\eta_1)}{a(\eta_1)} \right) \Delta\eta_j^2 + \int_{\eta_j}^{\eta_0} (\phi' - \psi') d\eta \right. \\ & \left. + \psi(\eta_0, \mathbf{x}(\eta_0)) - \psi(\eta_j, \mathbf{x}(\eta_j)) + \gamma \cdot \mathbf{v}_j + \frac{1}{2} |\mathbf{v}_j|^2 \right\}, \end{aligned} \quad (10)$$

where we introduced $a(\eta_1) = 1/(1 + z_1)$. This is the redshift of the j th object. We neglected the Doppler effect of the peculiar motion of the observer because we consider the relative redshift of objects located in a small region on the well-subhorizon scales. The names of the terms in Eq. (10) are summarised in Table I. We also omit the integrated Sachs–Wolfe term and $\psi(\eta_0, \mathbf{x}(\eta_0))$ in Eq. (10) because we consider the relative redshift of well-subhorizon objects. The gravitational potential of the observer $\psi(\eta_0, \mathbf{x}(\eta_0))$ does not contribute to the final result of the relative redshift. Then, in the present paper, we consider

$$1 + z_j \simeq (1 + z_1) \left\{ 1 - \mathcal{H}(\eta_1)\Delta\eta_j + \left(\mathcal{H}^2(\eta_1) - \frac{1}{2} \frac{a''(\eta_1)}{a(\eta_1)} \right) \Delta\eta_j^2 - \psi(\eta_j, \mathbf{x}(\eta_j)) + \gamma \cdot \mathbf{v}_j + \frac{1}{2} |\mathbf{v}_j|^2 \right\}. \quad (11)$$

The gravitational redshift of the reference object is expressed as

$$1 + z_r \simeq (1 + z_1) \left\{ 1 - \psi(\eta_1, \mathbf{x}(\eta_1)) + \int_{\eta_1}^{\eta_0} (\phi' - \psi') d\eta + \gamma \cdot \mathbf{v}_1 + \frac{1}{2} \mathbf{v}_1^2 \right\}. \quad (12)$$

For example, the reference object is the central galaxy in a halo in Sec. III. The difference between z_j and z_r is approximately given by

$$\delta z_{jr} \equiv z_j - z_r \simeq (1 + z_1) \left\{ \psi(\eta_1, \mathbf{x}(\eta_1)) - \psi(\eta_j, \mathbf{x}(\eta_j)) + \boldsymbol{\gamma} \cdot \mathbf{v}_j + \frac{1}{2} \mathbf{v}_j^2 - \boldsymbol{\gamma} \cdot \mathbf{v}_1 - \frac{1}{2} \mathbf{v}_1^2 \right\}. \quad (13)$$

In this expression, we omitted the Hubble term. This is the basic formula adopted in Sec. III in the present paper (cf. Refs. [11, 13]). However, the reference object is not necessarily introduced in Secs. IV and V, where we use Eq. (11).

When we consider clusters of galaxies as in Secs. III and IV, we omit the Hubble term in Eq. (11). This omission is justified for clusters of galaxies because galaxy clusters do not expand. On the contrary, we include the Hubble term when we consider voids in Sec. V.

In the next sections we consider applications of this section. In these analyses, the observational quantities are obtained by averaging the redshifts of objects over the velocity space with the phase space distribution function of objects $f(\mathbf{x}, \mathbf{v})$, which is defined on the lightcone coordinate (see Figure 2). The phase space distribution function $f(\mathbf{x}, \mathbf{v})$ on the lightcone coordinate is nontrivially related to the reference frame phase space distribution function $f_{\text{RF}}(t, \mathbf{x}, \mathbf{v})$ by

$$f(\mathbf{x}, \mathbf{v}) = (1 + \boldsymbol{\gamma} \cdot \mathbf{v}) f_{\text{RF}}(t, \mathbf{x}, \mathbf{v}) \Big|_{\text{light cone}}. \quad (14)$$

The reason why the phase space distribution function on the lightcone coordinate depends on the velocity in an asymmetric way with respect to $\boldsymbol{\gamma} \cdot \mathbf{v}$ is understood with Figure 2 (see the caption). Kaiser pointed out that this fact gives rise to an additional second-order Doppler term $\langle (\boldsymbol{\gamma} \cdot \mathbf{v})^2 \rangle$ in the process of averaging the redshifts over velocity space. We further average the redshifts over spatial coordinates depending on the situation and the measurement strategy used for the gravitational redshift, where the spatial coordinates consist of the radial coordinate of the line-of-sight direction, χ , and the coordinates \mathbf{x}_\perp , perpendicular to χ . In Sec. III, we perform an average over χ and \mathbf{x}_\perp , while, in Secs. IV and V, we perform an average only over χ in some ranges. In the present paper, for simplicity, we neglect the surface brightness modulation effect [11, 12].

III. SATELLITE GALAXIES VIRIALISED IN HALOS

The authors of Refs. [9, 10, 12] have reported measurements of the gravitational redshift of galaxies in and near clusters relative to bright cluster galaxies, which we revisit in this section. Here we restrict satellite galaxies virialised in a halo, and we develop a simple model of the gravitational redshift relative to central galaxies. Our model is based on the halo approach, which is useful for describing the distribution of the dark matter as well as galaxies from large scales to small scales [16–18]. Here we adopt the halo approach with central galaxies and satellite galaxies that fits the clustering of galaxies in redshift space [19–24]. We assume that the central galaxies are located at the centre of halos with negligible velocity dispersion and that the satellite galaxies are off-centred and moving with large virial random velocity.

Applying the result in the previous section, we regard the j th object as a satellite galaxy and the reference object as the central galaxy in a halo. Then, we take the following average of the redshift (13) over the satellite galaxies with the phase space distribution function $f(\mathbf{x}, \mathbf{v})$:

$$\langle \delta z \rangle = \frac{\int d^2 x_\perp \int d\chi \int d^3 v_j \delta z_{jr} f(\mathbf{x}, \mathbf{v}_j)}{\int d^2 x_\perp \int d\chi \int d^3 v_j f(\mathbf{x}, \mathbf{v}_j)}. \quad (15)$$

We take the effect of the lightcone coordinate by using Eq. (14), and we assume $\int d\chi \int d^3 v_j (\boldsymbol{\gamma} \cdot \mathbf{v}_j) f_{\text{RF}}(\mathbf{x}, \mathbf{v}_j) = 0$

TABLE I: Names of the terms in Eq. (10).

$-(1 + z_1) \mathcal{H}(\eta_1) \Delta \eta_j$	(first-order) Hubble term
$(1 + z_1) (\mathcal{H}^2 - a''/2a) _{\eta=\eta_1} \Delta \eta_j^2$	(second-order) Hubble term
$(1 + z_1) \int_{\eta_j}^{\eta_0} (\phi' - \psi') d\eta$	integrated Sachs–Wolfe term
$-(1 + z_1) \psi(\eta_j, \mathbf{x}(\eta_j))$	gravitational potential term
$(1 + z_1) \boldsymbol{\gamma} \cdot \mathbf{v}_j$	(first-order) Doppler term
$(1 + z_1) \mathbf{v}_j ^2 / 2$	(second-order) Doppler term

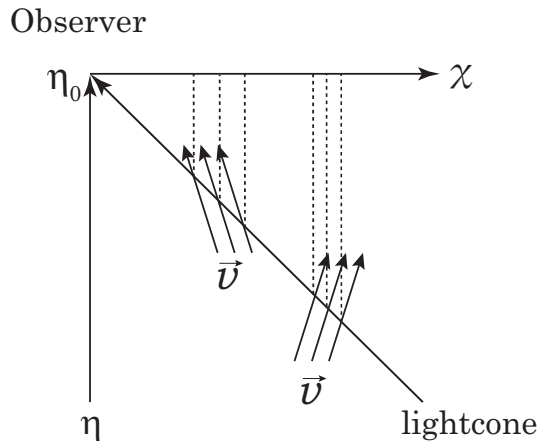


FIG. 2: A sketch to explain the lightcone effect on the phase-space distribution function. Even when the density of objects in the reference frame is the same, the density defined on the lightcone coordinate χ , which is obtained by projecting the points on which the objects intersect with the lightcone χ , depend on the velocity \mathbf{v} of the objects in an asymmetric way with respect to $\boldsymbol{\gamma} \cdot \mathbf{v}$.

owing to the spherical symmetry of the system statistically. Then, Eq. (15) leads to

$$\langle \delta z \rangle = (1 + z_1) \left(\psi(0) - \langle \psi_j \rangle + \langle (\boldsymbol{\gamma} \cdot \mathbf{v}_j)^2 \rangle + \frac{1}{2} \langle |\mathbf{v}_j|^2 \rangle \right), \quad (16)$$

where $\psi(0)$ denotes the gravitational potential at the centre of a halo and $\langle \psi_j \rangle$ denotes the expectation value of the gravitational potential of satellite galaxies and where $\langle (\boldsymbol{\gamma} \cdot \mathbf{v}_j)^2 \rangle$ and $\langle |\mathbf{v}_j|^2 \rangle$ denote the variance of the random velocity of satellite galaxies in one dimension and in three dimensions, respectively. These quantities are defined under the condition that the mass of a halo is fixed. Here we omitted the random velocity of the central galaxies by assuming that it is negligibly small compared with that of the satellite galaxies. We also omitted the Hubble terms. Assuming isotropy of the random velocity of satellite galaxies, $\langle (\boldsymbol{\gamma} \cdot \mathbf{v}_j)^2 \rangle = \langle \mathbf{v}_j^2 \rangle / 3$, we have

$$\langle \delta z \rangle = (1 + z_1) \left(\psi(0) - \langle \psi_s \rangle + \frac{5}{2} \langle (\boldsymbol{\gamma} \cdot \mathbf{v}_j)^2 \rangle \right). \quad (17)$$

When we take the random velocity of the central galaxies into account, $\langle (\boldsymbol{\gamma} \cdot \mathbf{v}_j)^2 \rangle$ is replaced by $\langle (\boldsymbol{\gamma} \cdot \mathbf{v}_j)^2 \rangle - \langle (\boldsymbol{\gamma} \cdot \mathbf{v}_1)^2 \rangle$, where $\langle (\boldsymbol{\gamma} \cdot \mathbf{v}_1)^2 \rangle$ is the one-dimensional velocity variance of a central galaxy.

For the one-dimensional random velocity variance of satellite galaxies, we here adopt the simplest model, following Refs. [21, 23, 24]:

$$\langle (\boldsymbol{\gamma} \cdot \mathbf{v}_j)^2 \rangle = \sigma_{\mathbf{v}, \text{off}}^2(M_{\text{vir}}) = \frac{GM_{\text{vir}}}{2R_{\text{vir}}}, \quad (18)$$

where r_{vir} and M_{vir} are the virial radius and the virial mass, respectively. We assume that the density profile of halos follows the NFW profile [25]

$$\rho_{\text{NFW}}(r) = \frac{\rho_s}{(r/r_s)(1 + r/r_s)^2}, \quad (19)$$

where ρ_s and r_s are the parameters. The gravitational potential ψ follows the Poisson equation

$$\Delta \psi(r) = 4\pi G \rho_{\text{NFW}}(r), \quad (20)$$

which leads to the solution

$$\psi(r) = -4\pi G \rho_s r_s^2 \frac{\ln(1 + r/r_s)}{(r/r_s)}. \quad (21)$$

We also assume that the satellite galaxy number density is proportional to the NFW profile. In this case, we may write

$$\begin{aligned}
\langle \psi_s \rangle &= 4\pi \int_0^{r_{\text{vir}}} dr r^2 \frac{\rho_{\text{NFW}}(r)}{M_{\text{vir}}} \psi(r) \\
&= \frac{4\pi r_s^3 \rho_s}{M_{\text{vir}}} (-4\pi G \rho_s r_s^2) \int_0^c dx \frac{\ln(1+x)}{(1+x)^2} \\
&= -\frac{c}{m^2(c)} \frac{c - \log(1+c)}{1+c} \frac{GM_{\text{vir}}}{r_{\text{vir}}}.
\end{aligned} \tag{22}$$

We introduce the concentration parameter c and the virial mass M_{vir} instead of ρ_s and r_s , by $c = r_{\text{vir}}/r_s$ and $M_{\text{vir}} = M(< r_{\text{vir}}) = 4\pi r_{\text{vir}}^3 \Delta_{\text{vir}} \bar{\rho}_m / 3$, where $M(< r_{\text{vir}})$ is the mass within the radius r_{vir} , $\bar{\rho}_m$ is the mean matter density, and Δ_{vir} is the density contrast of a halo, for which we here adopt $\Delta_{\text{vir}} = 265$ at $z = 0.3$. From Eq. (21) we have

$$\psi(0) = -4\pi G \rho_s r_s^2 = -\frac{GM_{\text{vir}}}{r_{\text{vir}}} \frac{c}{m(c)}. \tag{23}$$

where we defined $m(c) = \ln(1+c) - c/(1+c)$, and

$$\psi(0) - \langle \psi_s \rangle = \frac{GM_{\text{vir}}}{r_{\text{vir}}} \left(-\frac{c}{m(c)} + \frac{c}{m^2(c)} \frac{(c - \log(1+c))}{1+c} \right). \tag{24}$$

Combining the results, we have

$$\begin{aligned}
\langle \delta z \rangle &= (1+z_1) (\psi(0) - \langle \psi_s \rangle + \langle (\boldsymbol{\gamma} \cdot \mathbf{v}_j)^2 \rangle) \\
&= (1+z_1) \frac{GM_{\text{vir}}}{r_{\text{vir}}} \left(-\frac{c}{m(c)} + \frac{c}{m^2(c)} \frac{(c - \log(1+c))}{1+c} + \frac{5}{4} \right).
\end{aligned} \tag{25}$$

In the latter part of this section, we present a theoretical prediction with the halo occupation distribution with central galaxy and satellite galaxy. Note that $\langle \delta z \rangle$ of Eq. (25) is a function of the halo mass M_{vir} , which we write as $\langle \delta z(M_{\text{vir}}) \rangle$. Hereafter we write M_{vir} as M . In a practical analysis, we need to use a large number of satellite galaxies in different halo masses. We investigate the theoretical expectation value of the gravitational redshift by integrating over the halo mass function with the HOD for satellite galaxies. We follow the HOD fitting functions for the central galaxies and the satellite galaxies proposed in Ref. [19]:

$$N_{\text{HOD}}(M) = \langle N_{\text{cen}} \rangle (1 + \langle N_{\text{sat}} \rangle), \tag{26}$$

$$\langle N_{\text{cen}} \rangle = \frac{1}{2} \left[1 + \text{erf} \left(\frac{\log_{10}(M) - \log_{10}(M_{\text{min}})}{\sigma_{\log M}} \right) \right], \tag{27}$$

$$\langle N_{\text{sat}} \rangle = \left(\frac{M - M_{\text{cut}}}{M_1} \right)^\alpha, \tag{28}$$

where $\text{erf}(x)$ is the error function.

Table II lists the HOD parameters for the three galaxy samples, the luminous red galaxy (LRG) sample of the Sloan Digital Sky Survey (SDSS) II [20], the low redshift (LOWZ) sample [26], and the CMASS sample [27] of the Baryon Oscillation Spectroscopy Survey (BOSS) SDSS III. We assume that the mean redshifts of these galaxy samples are $z_{\text{mean}} = 0.32$ for the LRG sample and the LOWZ sample and $z_{\text{mean}} = 0.56$ for the CMASS sample.

The halo mass function dn/dM is the number density of halos with mass M per unit volume and per unit mass. Namely, the halo mass function $(dn/dM)dM$ describes the comoving number density of halos of the mass in the range $M \sim M + dM$. A fitting function of the halo mass function has been investigated with numerical simulations by several authors, fitted in the form [28–30]

$$M \frac{dn}{dM} = \frac{\bar{\rho}_m}{M} \frac{d \ln \sigma_R^{-1}}{d \ln M} f(\sigma_R), \tag{29}$$

where σ_R is the root-mean-square fluctuation in spheres containing mass M at the initial time, which is extrapolated to redshift z using linear theory, δ_c is the critical value of the initial overdensity that is required for collapse, and $\delta_c = 1.69$ is adopted. In the present paper, we adopt the fitting formula in Ref. [28]:

$$f(\sigma_R) = 0.322 \sqrt{\frac{2 \times 0.707}{\pi}} \left[1 + \left(\frac{\sigma_R}{0.707 \delta_c} \right)^{0.3} \right] \frac{\delta_c}{\sigma_R} \exp \left(-\frac{0.707 \delta_c^2}{2 \sigma_R^2} \right). \tag{30}$$

TABLE II: HOD parameters and the mean redshift for the LRG samples [20], the LOWZ sample [26], and the CMASS (mock) sample [27]. The mean redshift is used as the value of z_1 .

	LRG	LOWZ	CMASS
M_{\min}	$5.7 \times 10^{13} h^{-1} M_{\odot}$	$1.5 \times 10^{13} h^{-1} M_{\odot}$	$1.2 \times 10^{13} h^{-1} M_{\odot}$
$\sigma_{\log M}$	0.7	0.45	0.596
M_{cut}	$3.5 \times 10^{13} h^{-1} M_{\odot}$	$1.4 \times 10^{13} h^{-1} M_{\odot}$	$1.2 \times 10^{13} h^{-1} M_{\odot}$
M_1	$3.5 \times 10^{14} h^{-1} M_{\odot}$	$1.3 \times 10^{14} h^{-1} M_{\odot}$	$1.0 \times 10^{14} h^{-1} M_{\odot}$
α	1	1.38	1.0
mean redshift	0.32	0.32	0.56

TABLE III: Contributions of the gravitational potential $(1+z_1)(\psi(0) - \langle\psi_s\rangle)$, the Doppler term $(1+z_1)\frac{5}{2}\langle(\boldsymbol{\gamma} \cdot \boldsymbol{v})^2\rangle$, and the total $\langle\delta z\rangle$ for the LRG sample, the LOWZ sample, and the CMASS sample. Note that \bar{r}_{vir} shows the averaged virial radius for each galaxy sample.

	LRG	LOWZ	CMASS
$(1+z_1)(\psi(0) - \langle\psi_s\rangle)$	-3.2×10^{-5} (−9.7 km/s)	-2.3×10^{-5} (−7.0 km/s)	-1.8×10^{-5} (−5.4 km/s)
$(1+z_1)\frac{5}{2}\langle(\boldsymbol{\gamma} \cdot \boldsymbol{v})^2\rangle$	$+1.7 \times 10^{-5}$ (+5.1 km/s)	$+1.2 \times 10^{-5}$ (+3.5 km/s)	$+1.0 \times 10^{-5}$ (+3.0 km/s)
$\langle\delta z\rangle$	-1.5×10^{-5} (−4.6 km/s)	-1.2×10^{-5} (−3.5 km/s)	-0.8×10^{-5} (−2.5 km/s)
\bar{r}_{vir}	$1.0 h^{-1} \text{Mpc}$	$0.85 h^{-1} \text{Mpc}$	$0.79 h^{-1} \text{Mpc}$

TABLE IV: Same as Table III, but for the modified gravity case with the effective gravitational constant $G_{\text{eff}} = 4G/3$, which only modifies the velocity dispersion of satellite galaxies.

	LRG	LOWZ	CMASS
$(1+z_1)(\psi(0) - \langle\psi_s\rangle)$	-3.2×10^{-5} (−9.7 km/s)	-2.3×10^{-5} (−7.0 km/s)	-1.8×10^{-5} (−5.4 km/s)
$(1+z_1)\frac{5}{2}\langle(\boldsymbol{\gamma} \cdot \boldsymbol{v})^2\rangle$	$+2.3 \times 10^{-5}$ (+6.8 km/s)	$+1.6 \times 10^{-5}$ (+4.7 km/s)	$+1.3 \times 10^{-5}$ (+3.9 km/s)
$\langle\delta z\rangle$	-1.0×10^{-5} (−3.0 km/s)	-0.8×10^{-5} (−2.3 km/s)	-0.5×10^{-5} (−1.5 km/s)

TABLE V: Same as Table III, but for the case in which the central galaxies have a random velocity with 30% of that of the satellite galaxies.

	LRG	LOWZ	CMASS
$(1+z_1)(\psi(0) - \langle\psi_s\rangle)$	-3.2×10^{-5} (−9.7 km/s)	-2.3×10^{-5} (−7.0 km/s)	-1.8×10^{-5} (−5.4 km/s)
$(1+z_1)\frac{5}{2}\langle(\boldsymbol{\gamma} \cdot \boldsymbol{v})^2\rangle$	$+1.5 \times 10^{-5}$ (+4.6 km/s)	$+1.1 \times 10^{-5}$ (+3.2 km/s)	$+0.9 \times 10^{-5}$ (+2.7 km/s)
$\langle\delta z\rangle$	-1.7×10^{-5} (−5.1 km/s)	-1.3×10^{-5} (−3.8 km/s)	-0.9×10^{-5} (−2.8 km/s)

We compute the ensemble average of the gravitational redshift over the halo mass function with the satellite galaxy HOD by using

$$\langle\delta z\rangle = \frac{\int dM \frac{dn}{dM} \langle N_{\text{sat}} \rangle \delta z(M)}{\int dM \frac{dn}{dM} \langle N_{\text{sat}} \rangle}, \quad (31)$$

where we insert Eq. (25) into the right-hand-side of Eq. (31). Table III lists the result of $\langle\delta z\rangle$, which is the combination of the gravitational potential term $(1+z_1)(\psi(0) - \langle\psi_s\rangle)$ and the second-order Doppler terms $(1+z_1)\frac{5}{2}\langle(\boldsymbol{\gamma} \cdot \boldsymbol{v})^2\rangle$, for each galaxy sample. The result shows that the gravitational potential term $(1+z_1)(\psi(0) - \langle\psi_s\rangle)$ is the order of a few $\times 10^{-5}$, while the second-order Doppler term $\langle(\boldsymbol{\gamma} \cdot \boldsymbol{v})^2\rangle$ makes a significant contribution, and the total amplitude of the signal is significantly reduced. Because we consider the satellite galaxies virialised in halos, the typical separation between the central galaxy and the satellite is the virial radius of the order of $1 h^{-1} \text{Mpc}$, where the second-order Doppler term makes a significant contribution to the total amplitude of the signal. In the velocity unit, the amplitude of the signal is from 5 to 2 km/s depending on the samples. This is consistent with previous results [9, 10, 12]. The result also

shows that the amplitude of the signal decreases from left to right in Table III. This HOD dependence is understood as the change of an averaged size of halos for each galaxy sample. The averaged virial radius \bar{r}_{vir} , which is defined similarly to Eq. (31), decreases from left to right in Table III, which means that the gravitational potential of satellite galaxies becomes shallower accordingly.

An interesting application of measurements of the gravitational redshift is the testing modified gravity models. For example, in an $F(R)$ gravity model, when the screening mechanism does not work, the velocity of satellite galaxies increases owing to the scalar force. However, the gravitational potential does not change as long as the matter density profile is the same. When the effective gravitational constant as well as the variance of the random velocity increases by the factor 4/3, the signal of the gravitational redshift is evaluated as indicated in Table IV. This demonstrates that the gravitational redshift is potentially an interesting test of modified gravity [10]. However, the random velocity of central galaxies could be a systematic error [9, 10, 12]. When the central galaxy has a random velocity dispersion of 30% of the satellite galaxies, the prediction changes, as shown in Table V. Thus, we need further investigations of the errors and systematics of the method as a test of gravity theories.

We simply estimate the error of the averaged central-satellite velocity difference $\Delta v^{\text{cen-sat}}$ in a given galaxy samples by inverse-variance weighted averaging as follows:

$$(\Delta v^{\text{cen-sat}})^{-2} = V \int dM \frac{dn}{dM} \langle N_{\text{cen}} \rangle \langle N_{\text{sat}} \rangle \sigma_{\text{vir}}^{-2}, \quad (32)$$

where V is the survey volume, σ_{vir} is the Virial velocity of the host halo with mass M and we set $V = 1.6(h^{-1}\text{Gpc})^2$ for SDSS LRG, $V = 0.79(h^{-1}\text{Gpc})^2$ for LOWZ, and $V = 1.75(h^{-1}\text{Gpc})^2$ for CMASS samples. We find that $\Delta v^{\text{cen-sat}}$ becomes 5.0 km/s (SDSS LRG), 2.7 km/s (LOWZ), and 1.4 km/s (CMASS). The signal-to-noise ratio of δz is 1–2 in the current sample. The statistical error will be improved in future galaxy surveys such as DESI, PFS, and Euclid, which cover a larger survey volume. Here we assume that all of the central galaxies are identified. The gravitational redshift signal weakens depending on the fraction of misidentified central galaxies.

IV. INTRACLUSTER GAS

The recent studies of the gravitational redshift of clusters galaxies focused on measurements of galaxies [9–13]. Motivated by the recent X-ray observations by the Hitomi satellite, in which intracluster gas motions were investigated with an accuracy of the order of 10 to 20 km/s, we next consider the gravitational redshift of intracluster gas. The gravitational redshift of X-ray gas was investigated in Ref. [31], but we here explain another motivation for considering this problem. Nonthermal pressure of the intracluster gas is an unsolved problem in cluster physics. From cosmological hydrodynamical simulations, it is shown that intracluster gas motions can be generated in the structure formation process and that nonthermal random motions contribute to the nonthermal pressure (e.g., [33, 34]). This nonthermal pressure might cause a discrepancy between the hydro-equilibrium mass and the lensing mass. In this section, we assume that small-scale random motions of intracluster gas cause the nonthermal pressure, and we investigate a possible signal of the gravitational redshift based on a simple model of the intracluster gas including the nonthermal pressure.

We start by assuming that intracluster gas particles follow the Boltzmann distribution function (e.g., [32])

$$f_{\text{RF}}(\mathbf{x}, \mathbf{v}) = n(\mathbf{x}) \left(\frac{2\pi}{mT(\mathbf{x})} \right)^{3/2} \exp \left\{ -m \frac{[\mathbf{v} - \mathbf{V}(\mathbf{x})]^2}{2T(\mathbf{x})} \right\}, \quad (33)$$

which is characterised by particle number density $n(\mathbf{x})$ of a specific element at position \mathbf{x} , temperature $T(\mathbf{x})$, the peculiar velocity field of the random motions, $\mathbf{V}(\mathbf{x})$, and the mass of the particle, m , where we consider iron particles. Here we adopt units in which the Boltzmann constant equals one.

From Eq. (11), omitting the Hubble term, we can write the redshift of a particle as

$$1 + z_j \simeq 1 + z_1 + (1 + z_1) \left\{ -\psi(\eta_j, \mathbf{x}(\eta_j)) + \boldsymbol{\gamma} \cdot \mathbf{v}_j + \frac{1}{2} v_j^2 \right\}. \quad (34)$$

Then, we define the gravitational redshift projected along the line-of-sight direction by integrating Eq. (34) over velocity space and the line-of-sight coordinate:

$$1 + \langle z(x_{\perp}) \rangle = 1 + z_1 + (1 + z_1) \frac{\int d\chi \int d^3v f(\mathbf{x}, \mathbf{v}) (\boldsymbol{\gamma} \cdot \mathbf{v} + \frac{1}{2} v^2 - \psi(\mathbf{x}))}{\int d\chi \int d^3v f(\mathbf{x}, \mathbf{v})}. \quad (35)$$

After integration with respect to the velocity, we have

$$1 + \langle z(x_\perp) \rangle = 1 + z_1 + (1 + z_1) \frac{\int d\chi n(\mathbf{x}) \left\{ \boldsymbol{\gamma} \cdot \mathbf{V}(\mathbf{x}) + (\boldsymbol{\gamma} \cdot \mathbf{V}(\mathbf{x}))^2 + \frac{1}{2} |\mathbf{V}(\mathbf{x})|^2 + \frac{5}{2} \frac{T(\mathbf{x})}{m} - \psi(\mathbf{x}) \right\}}{\int d\chi n(\mathbf{x}) (1 + \boldsymbol{\gamma} \cdot \mathbf{V})}. \quad (36)$$

If we assume that the system is spherically symmetric, we may omit the linear term $\int d\chi n(\mathbf{x}) \boldsymbol{\gamma} \cdot \mathbf{V} = 0$. This assumption will not be justified when spherical symmetry of the system is not guaranteed. However, we may assume this spherical symmetry statistically when many clusters are observed. Then, we have

$$1 + \langle z_j(x_\perp) \rangle = 1 + z_1 + (1 + z_1) \frac{\int d\chi n(\mathbf{x}) \left((\boldsymbol{\gamma} \cdot \mathbf{V}(\mathbf{x}))^2 + \frac{1}{2} |\mathbf{V}(\mathbf{x})|^2 + \frac{5}{2} \frac{T(\mathbf{x})}{m} - \psi(\mathbf{x}) \right)}{\int d\chi n(\mathbf{x})}. \quad (37)$$

Here we assume isotropy of the peculiar velocity dispersion, $3\langle (\boldsymbol{\gamma} \cdot \mathbf{V})^2 \rangle = \langle |\mathbf{V}|^2 \rangle = \sigma_{\text{rnd}}^2$, where σ_{rnd}^2 denotes the variance of the random motions of the gas. Furthermore, by assuming that the emissivity of the photon line emission is proportional to the number density of particles, i.e., the mass density of gas particles, ρ_{gas} , Eq. (37) leads to

$$1 + \langle z(x_\perp) \rangle = 1 + z_1 + (1 + z_1) \frac{\int d\chi \rho_{\text{gas}}(\mathbf{x}) \left(\frac{5}{6} \sigma_{\text{rnd}}^2(\mathbf{x}) + \frac{5}{2} \frac{T(\mathbf{x})}{m} - \psi(\mathbf{x}) \right)}{\int d\chi \rho_{\text{gas}}(\mathbf{x})}. \quad (38)$$

Note that the right-hand side of Eq. (38) is a function of the projected radius χ_\perp , and we define the relative gravitational redshift by

$$\langle \delta z(x_\perp) \rangle = \langle z(x_\perp) \rangle - \langle z(0) \rangle. \quad (39)$$

When spherical symmetry of the system is guaranteed statistically, the integration of the term $\boldsymbol{\gamma} \cdot \mathbf{V}(\mathbf{x})$ in Eq. (36) becomes zero; otherwise, the term makes a large contribution. To estimate the variance of this term, for simplicity, we estimate the variance of δz by

$$\begin{aligned} \langle \delta z^2(x_\perp) \rangle &= (1 + z_1)^2 \left\langle \left(\frac{\int d\chi n(\mathbf{x}) (\boldsymbol{\gamma} \cdot \mathbf{V})}{\int d\chi n(\mathbf{x})} \right)^2 \right\rangle \\ &\simeq (1 + z_1)^2 \frac{\int d\chi n^2(\mathbf{x}) (\boldsymbol{\gamma} \cdot \mathbf{V})^2}{\int d\chi n^2(\mathbf{x})} = (1 + z_1)^2 \frac{\int d\chi \rho_{\text{gas}}^2(\mathbf{x}) \frac{1}{3} \sigma_{\text{rnd}}^2}{\int d\chi \rho_{\text{gas}}^2(\mathbf{x})}, \end{aligned} \quad (40)$$

where $\langle \cdot \rangle$ in the above equation means the ensemble average with respect to the random motions $\mathbf{V}(\mathbf{x})$.

In the latter part of this section, we demonstrate the contribution of the terms of Eq. (38) adopting a simple model of intracluster gas. The nonthermal pressure in intracluster gas is under debate based on cosmological hydrodynamical simulations (e.g., [33, 34]). Their simulation results indicate that small-scale random motions of intracluster gas are generated during the process of the cluster formation, which causes nonthermal pressure of the intracluster gas. We therefore assume that the small-scale random motions are responsible for the nonthermal pressure. Following this scenario, we adopt the following model of random velocity $\sigma_{\text{rnd}}^2(r)$ in connection with nonthermal pressure $P_{\text{nonthermal}}(r)$ [33–37]:

$$\rho_{\text{gas}}(r) \sigma_{\text{rnd}}^2(r) = P_{\text{nonthermal}}(r). \quad (41)$$

The nonthermal pressure is estimated by the fraction $g(r)$ of the total pressure:

$$P_{\text{nonthermal}}(r) = g(r) P_{\text{total}}(r). \quad (42)$$

Hence, using $P_{\text{total}} = g^{-1} P_{\text{nonthermal}} = (1 - g)^{-1} P_{\text{thermal}}$, we may write

$$P_{\text{nonthermal}}(r) = \frac{g(r)}{1 - g(r)} n_{\text{gas}}(r) T(r), \quad (43)$$

where we used $P_{\text{thermal}}(r) = n_{\text{gas}}(r) T(r)$, and $n_{\text{gas}}(r)$ is the number density of the particles in the intracluster gas. According to hydrodynamical simulations [33, 34], the nonthermal pressure component to the total pressure can be modelled with the expression

$$g(r) = \alpha_{nt} (1 + z)^{\beta_{nt}} \left(\frac{r}{r_{500}} \right)^{n_{nt}} \left(\frac{M_{200}}{3 \times 10^{14} M_\odot} \right)^{n_M}, \quad (44)$$

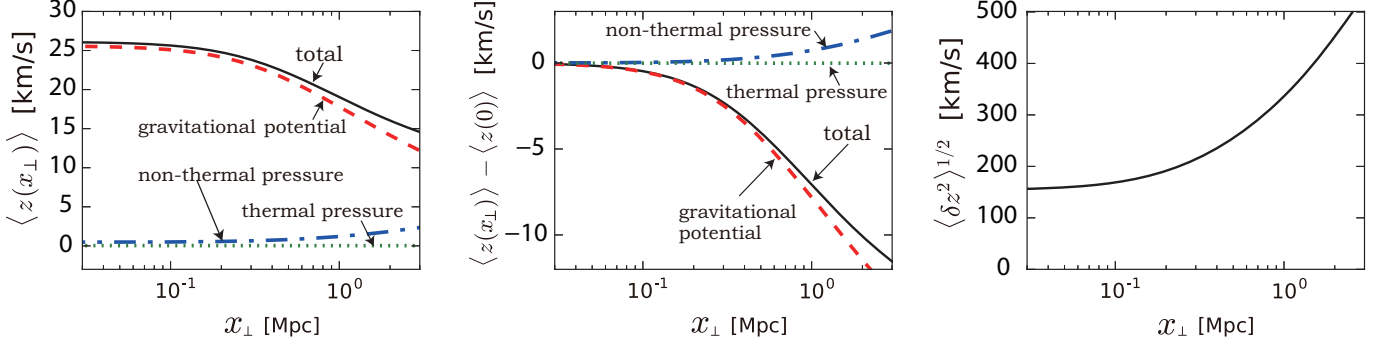


FIG. 3: Contribution to the gravitational redshift by adopting a model for the Coma Cluster (see the Appendix for details). *Left panel:* The black curve shows the total of $\langle z(x_\perp) \rangle$ of Eq. (38), the red dashed curve shows the gravitational potential term $\psi(\mathbf{x})$, the blue dash-dotted curve shows the nonthermal pressure term $5\sigma_{\text{rnd}}^2/6$, and the green dotted curve shows the thermal pressure term $5T(\mathbf{x})/2m$. *Middle panel:* The same as the left panel but for $\langle \delta z(x_\perp) \rangle = \langle z(x_\perp) \rangle - \langle z(0) \rangle$. *Right panel:* The variance $\sqrt{\langle \delta z^2(x_\perp) \rangle}$ of Eq. (40). In this figure, we adopted $z_1 = 0$.

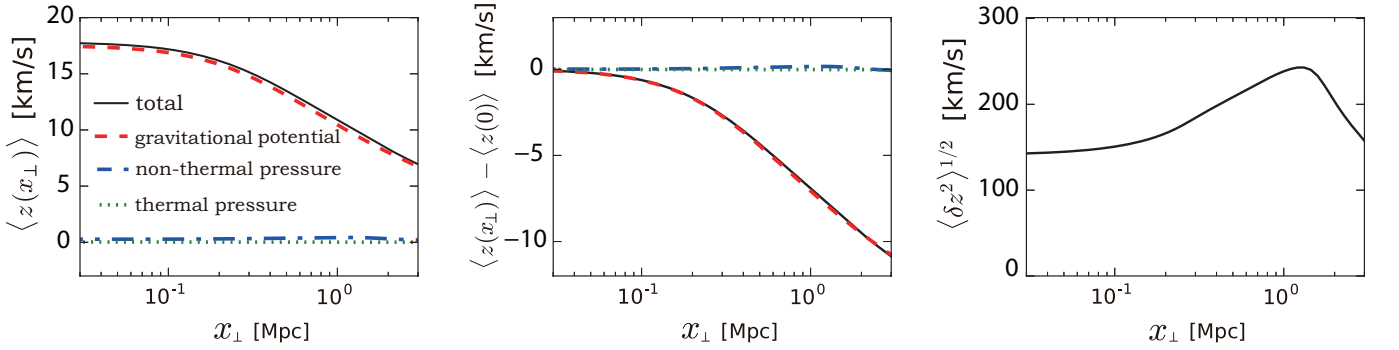


FIG. 4: Same as Fig. 3, but for the Perseus Cluster; the modelling parameters are from Urban et al. [48] and Simionescu et al. [51] (see also the Appendix).

where α_{nt} , β_{nt} , n_{nt} , and n_M are constants. Here r_{500} and M_{200} mean the radius and mass at the radius where the matter density in the galaxy cluster is 500 and 200 times of the critical density, respectively. For our demonstration of the effects from the nonthermal pressure contribution, we adopt the parameter values $(\alpha_{nt}, \beta_{nt}, n_{nt}, n_M) = (0.18, 0.5, 0.8, 0.2)$, which are the best-fit values of the numerical simulations in Ref. [34]. The value of α_{nt} determines the contribution from the random motions of gas, σ_{rnd}^2 .

Figures 3 and 4 exemplify the behaviour of $\langle z(x_\perp) \rangle$ (left panel) and $\langle \delta z(x_\perp) \rangle$ (centre panel) as a function of x_\perp on the basis of theoretical models for the Coma Cluster and the Perseus Cluster, respectively, which are constructed to fit observations. The details of the theoretical models are summarised in the Appendix. In the left and centre panels of these figures, the red dashed curve is the gravitational potential contribution, the blue dash-dotted curve is the nonthermal pressure term contribution, and the green dotted curve is the thermal pressure term contribution. The black solid curve is the total pressure. Thus, the amplitude of the relative gravitational redshift (centre panel) is of the order of 5–10 km/s. The gravitational potential term makes a dominant contribution to the gravitational redshift, though the nonthermal pressure term makes a slight contribution. The contribution from the thermal pressure is completely negligible. However, measurements of the outskirts region is necessary for detecting the signal of the relative gravitational redshift.

The right panels of Figs. 3 and 4 show $\langle \delta z^2(x_\perp) \rangle^{1/2}$, which can be interpreted as the dispersion of the signal in the x_\perp direction. When the random motions of gas have coherent large-scale structures in a halo, many clusters will be necessary to reduce the statistical errors for the measurement of the gravitational redshift. The error estimation will depend on the properties of the random motions of gas, which is beyond scope of the present paper.

V. VOID MODEL

We next consider a possible signal of the gravitational redshift in measurements of galaxies associated with voids. Voids are characteristic structures of the large-scale structure in the cold dark matter universe. Recently, voids have become a useful tool for testing cosmological models and gravity theories (e.g., see Refs. [38–43]).

In general, the region inside a void is not always completely empty, and some galaxies might be found inside voids. This gives us a chance to find a possible signal of the gravitational redshift of voids. However, in the case of voids, in contrast to the case of clusters of galaxies, a galaxy is not always found at the centre of a void. Then, as in the case of the previous section, we consider the projection along the line-of-sight direction, and we consider the relative gravitational redshift as a function of the projected radius, the coordinate perpendicular to the line-of-sight direction. We consider the average

$$\begin{aligned} 1 + \langle z(x_\perp) \rangle &= \frac{\int d\chi \int d^3v_j (1 + z_j) f(\mathbf{x}, \mathbf{v}_j)}{\int d\chi \int d^3v_j f(\mathbf{x}, \mathbf{v}_j)} \\ &= 1 + z_1 + (1 + z_1) \frac{\int d\chi n_g(\chi, x_\perp) \tilde{\delta}z(\chi, x_\perp)}{\int d\chi n_g(\chi, x_\perp) (1 + \boldsymbol{\gamma} \cdot \mathbf{V})}, \end{aligned} \quad (45)$$

where $n_g(\chi, x_\perp)$ is the galaxy number density, and we defined

$$\tilde{\delta}z(\chi, x_\perp) = \left\{ -\mathcal{H}(\eta_1) \Delta\eta_j + \left(\mathcal{H}^2(\eta_1) - \frac{1}{2} \frac{a''(\eta_1)}{a(\eta_1)} \right) \Delta\eta_j^2 - \psi(\eta_j, \mathbf{x}(\eta_j)) + \boldsymbol{\gamma} \cdot \mathbf{V} + (\boldsymbol{\gamma} \cdot \mathbf{V})^2 + \frac{1}{2} |\mathbf{V}|^2 \right\}, \quad (46)$$

where \mathbf{V} is the peculiar velocity, which should be understood as $\mathbf{V} = \mathbf{V}(\eta_j, \mathbf{x}(\eta_j))$. In the case of a void, we include the Hubble term because the void is a cosmological structure distributed on larger scales compared with a cluster of galaxies.

By assuming spherical symmetry of the system statistically, the linear terms in \mathbf{V} and $\Delta\eta_j$ vanish, i.e., $\int d\chi n_g \boldsymbol{\gamma} \cdot \mathbf{V} = \int d\chi n_g \Delta\eta_j = 0$, and we have

$$1 + \langle z(x_\perp) \rangle = 1 + z_1 + (1 + z_1) \frac{\int d\chi n_g(\chi, x_\perp) \tilde{\delta}z(\chi, x_\perp)}{\int d\chi n_g(\chi, x_\perp)} \quad (47)$$

with

$$\tilde{\delta}z(\chi, x_\perp) = \left\{ \left(\mathcal{H}^2(\eta_1) - \frac{1}{2} \frac{a''(\eta_1)}{a(\eta_1)} \right) \Delta\eta_j^2 - \psi(\eta_j, \mathbf{x}(\eta_j)) + (\boldsymbol{\gamma} \cdot \mathbf{V})^2 + \frac{1}{2} |\mathbf{V}|^2 \right\}, \quad (48)$$

where we should understand that $\mathbf{x} = (\chi, \mathbf{x}_\perp)$. We need to perform the projection along the line-of-sight direction, i.e., integration of $\tilde{\delta}z(\chi, x_\perp)$ over the line-of-sight coordinate χ in some range with fixed x_\perp , and we consider the relative gravitational redshift defined by

$$\langle z(x_\perp) \rangle - \langle z(0) \rangle = (1 + z_1) \frac{\int d\chi n_g(\chi, x_\perp) \tilde{\delta}z(\chi, x_\perp)}{\int d\chi n_g(\chi, x_\perp)} - (1 + z_1) \frac{\int d\chi n_g(\chi, 0) \tilde{\delta}z(\chi, 0)}{\int d\chi n_g(\chi, 0)}. \quad (49)$$

In the latter part of this section, we demonstrate a possible signal of the gravitational potential in the redshift of galaxies associated with voids. We here adopt the simple model for a spherically symmetric void in Ref. [42], where the integrated density contrast of matter is given in the form

$$\Delta(r) = \Delta_c e^{-(r/r_v)^\alpha}, \quad (50)$$

where Δ_c , r_v , and α are the parameters. Δ_c specifies the amplitude of the density contrast, r_v is the characteristic radius, and α characterises the steepness of the void wall. This void profile is quite simple, however, it is used in the analysis of voids in Ref. [42], which demonstrates that it works in a practical analysis. In the present paper, we adopt $\Delta_c = -0.8$ and $\alpha = 3$. Here $\Delta(r)$ is related to the matter density contrast $\delta(r)$ and the gravitational potential ψ by

$$\Delta(r) = \frac{3}{r^3} \int_0^r dr' r'^2 \delta(r'), \quad (51)$$

$$\Delta\psi(r) = 4\pi G a^2 \bar{\rho}_m(a) \delta(r), \quad (52)$$

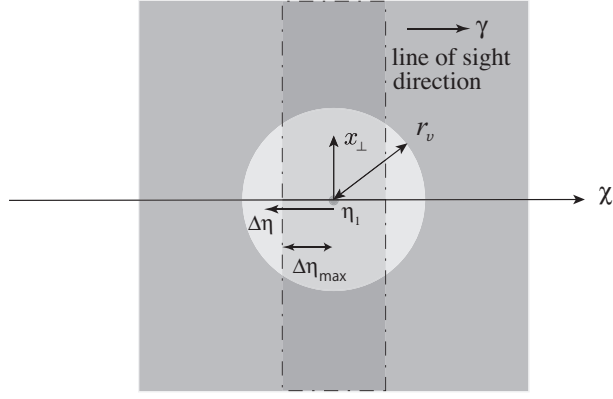


FIG. 5: Galaxies in the region surrounded by the dash-dotted line are used for the (projection) analysis, and we perform the integration over χ (projection along the line-of-sight direction) by fixing x_{\perp} , where χ and $\Delta\eta$ are related by $\chi = \eta_0 - \eta = \eta_0 - \eta_1 - \Delta\eta$.

where $\bar{\rho}_m(a)$ is the background matter density. Assuming a spatially flat cosmology with a cosmological constant, we may write $\bar{\rho}_m(a) = 8\pi G\Omega_m H_0^2/3a^3$, where Ω_m is the density parameter and H_0 is the Hubble parameter at the present epoch. Then, the density contrast and the gravitational potential of the model are given by

$$\delta(r) = \frac{1}{r^2} \frac{d}{dr} \left(\frac{r^3 \Delta(r)}{3} \right) = \Delta_c \left(1 - \frac{\alpha}{3} \left(\frac{r}{r_v} \right)^\alpha \right) e^{-(r/r_v)^\alpha}, \quad (53)$$

$$\psi(r) = -\frac{3\Omega_m H_0^2}{2a} \int_r^\infty dr' r' \frac{\Delta(r')}{3} = -\frac{H_0^2 r_v^2}{2} \frac{\Omega_m \Delta_c}{\alpha a} \Gamma(2/\alpha, (r/r_v)^\alpha), \quad (54)$$

where $\Gamma(z, a)$ is the incomplete Gamma function.

By solving the continuity equation, the peculiar velocity of the radial direction can be written (see, e.g., Ref.[42]) as

$$V(r) = -\mathcal{H}r\Delta(r)\frac{f(a)}{3}, \quad (55)$$

where $f(a) = d \ln D_1(a)/d \ln a$ is the growth rate defined by logarithmic differentiation with respect to the scale factor a , which is approximately written as $f(a) = [\Omega_m(a)]^\gamma$ with $\Omega_m(a) = a^{-3}\Omega_m/(a^{-3}\Omega_m + 1 - \Omega_m)$ and $\gamma = 0.55$. In the present paper, we assume that galaxies follow the matter peculiar velocity field.

Figure 6 shows each term in the expression of the relative gravitational redshift of Eq. (49) in the unit of km/s, which is normalised by $(1 + z_1)(r_v/30h^{-1}\text{Mpc})^2$ as functions of x_{\perp}/r_v . In each panel, the red dashed curve is the gravitational potential term, the green dotted curve is the Hubble term, blue dash-dotted is the Doppler term, and the black solid curve is the total gravitational redshift. We find that the amplitude of the gravitational redshift of voids is

$$\langle z(x_{\perp}) \rangle - \langle z(0) \rangle \sim -\mathcal{O}(0.1) \times (H_0 r_v)^2 (1 + z_1) \sim -\mathcal{O}(10^{-6}) \times \left(\frac{r_v}{10 h^{-1} \text{Mpc}} \right)^2 (1 + z_1). \quad (56)$$

The signal changes depending on the range of the projection. Each panel of Fig. 6 depicts a different range of the projection along the line-of-sight direction. When the range of the projection is narrow, the gravitational potential term dominates the gravitational redshift. However, when the range of the projection is wide, the second-order Hubble term makes a large contribution. Thus, the amplitude of the signal of the gravitational redshift of voids changes depending on the range of the projection along the line-of-sight direction. When the background expansion of the universe is well determined, we might be able to subtract the dominant contribution from the second-order Hubble term in an analysis with some calibration technique.

From Fig. 6, we find that the contribution from second order Doppler term (blue dash-dotted curve) is quite smaller than that from the gravitational potential term (red dashed curve). The amplitude of the gravitational potential term is typically several times larger than that of the second order Doppler term. Furthermore, the amplitude of the velocity of void is zero at the centre of voids, while the gravitational potential ψ has a finite value at the centre of voids. The integration of each term over χ makes the large difference between these two contributions in Fig. 6.

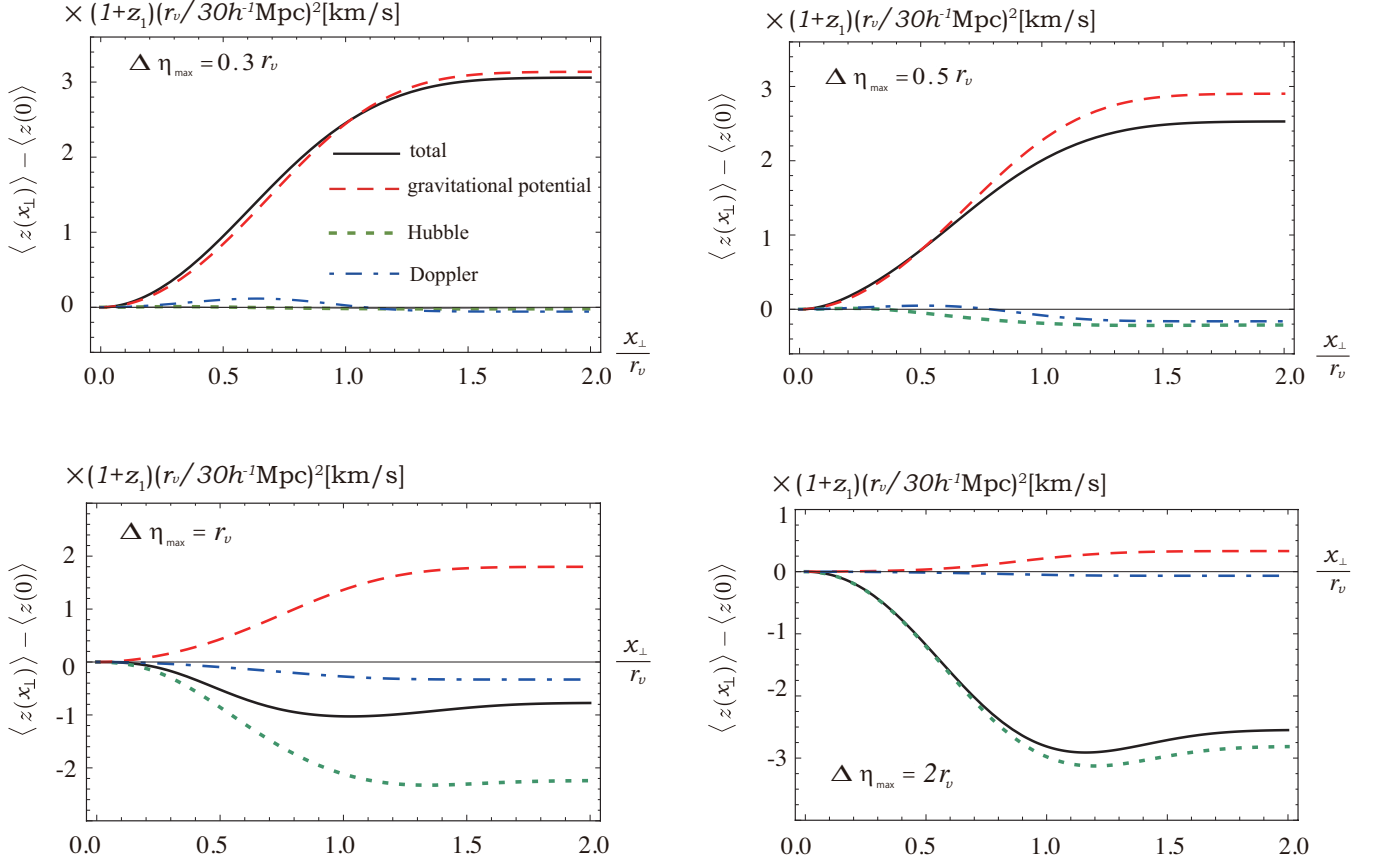


FIG. 6: Relative gravitational redshift $\langle z(x_\perp) \rangle - \langle z(0) \rangle$ in the unit of km/s, which is normalised by $(1+z_1)(r_v/30h^{-1}\text{km/s})^2$ as functions of x_\perp/r_v . The black solid curve is the total of $\langle z(x_\perp) \rangle - \langle z(0) \rangle$, the green dotted curve is the second-order Hubble term, the red dashed curve is the gravitational potential term, and the blue dash-dotted curve is the Doppler term contribution. In these plots, we adopted different ranges of the projection along the line-of-sight coordinate $\eta_1 - \Delta\eta_{\max} < \eta < \eta_1 + \Delta\eta_{\max}$ (see Fig. 5) with $\Delta\eta_{\max} = 0.3r_v$ (upper left panel), $\Delta\eta_{\max} = 0.5r_v$ (upper right panel), $\Delta\eta_{\max} = r_v$ (lower left panel), and $\Delta\eta_{\max} = 2r_v$ (lower right panel), respectively, where we adopted the parameters $\alpha = 3$, $\Delta_c = -0.8$, $\Omega_m = 0.3$, and $z_1 = 1$.

The gravitation redshifts of the order of a few km/s have been measured in the previous works using 10^5 galaxies associated with clusters [9, 10, 12]. Then, we think that it might be possible to detect the gravitational redshift of voids. However, the absence of a galaxy at the center of a void might cause a difficulty in the detection of the gravitational redshift of voids. In the case of cluster of galaxies, a central galaxy can be used to measure the relative redshift. In contrast, we cannot use such an object at the center of void. This is a difference which might make difficult to detect the gravitational redshift of voids. In the analysis in this section, we considered a simple method of averaging the redshifts of galaxies. A more sophisticated method to detect the signal of the gravitational potential of voids might be developed, although such investigation is beyond the scope of the present paper.

VI. SUMMARY AND CONCLUSIONS

We have investigated possible signals for the gravitational redshift in clusters and voids. Galaxies associated with clusters are the most promising objects for detecting the gravitational redshift, as demonstrated in previous works. With the use of the HOD description with central galaxies and satellite galaxies in a redshift survey, we have investigated the gravitational redshift of satellite galaxies virialised in halos relative to those of the central galaxies. In this model, the satellite galaxies are restricted to those located within the virial radius, which limits the information available compared with that of previous works. Our simple analytic model is useful for understanding how the gravitational redshift signal depends on the HOD properties of galaxy samples. The virialised random motions of satellite galaxies in halos makes a large contribution to the gravitational redshift through the second-order Doppler effect. This feature is potentially useful for testing modified gravity models.

We have also investigated the gravitational redshift in measurements of intracluster gas. Developing a simple model for the intracluster gas including the nonthermal pressure generated from the random motions proposed by numerical simulations, we evaluated a possible signal of the gravitational redshift of intracluster gas. The gravitational redshift is dominated by the gravitational potential term, but the nonthermal pressure term makes a slight contribution. For a detection of the relative gravitational redshift, measurements of the outskirts region are essential.

Finally, we have investigated the gravitational redshift of voids. Adopting a very simple model of a void profile, we obtained an analytic formula for the gravitational redshift. The amplitude of the signal is $\delta z = \mathcal{O}(1)\text{--}\mathcal{O}(10)$ km/s depending on the size of the void. The signal of the relative gravitational redshift depends on the range of the projection of galaxies along the line-of-sight direction. When the range of the projection is narrow, the gravitational potential term dominates the gravitational redshift. However, when the range of the projection is wide, the second-order Hubble term makes a large contribution. These results should be tested more carefully using mock catalogs and galaxy samples, including estimations of statistical and systematic errors.

Acknowledgments

We thank anonymous referee for the crucial comments on our first version of the manuscript, including pointing out our misunderstanding, which significantly improved this paper. This work is supported by MEXT/JSPS KAKENHI Grant Numbers 15H05895, 17K05444, and 17H06359 (KY). We thank N. Okabe, N. Werner, and Y. Fukazawa, B. Granett for useful communications. We also thank A. Taruya, S. Saito, N. Sugiyama, K. Koyama, D. Parkinson, and M. Sasaki for useful discussions and comments in the workshop YITP-T-17-03.

Appendix A: Model of intracluster gas

We assume the following equation of state for the thermal gas components in a cluster:

$$P_{\text{thermal}}(r) = n_{\text{gas}}(r)T_{\text{gas}}(r), \quad (\text{A1})$$

where we use a β -model for the three-dimensional electron number density profile [45],

$$n_{\text{gas}}(r) = n_0 \left[1 + \left(\frac{r}{r_c} \right)^2 \right]^{-3\beta/2}, \quad (\text{A2})$$

and the three-dimensional temperature profile,

$$T_{\text{gas}}(r) = \begin{cases} T_0 [1 + A(r/r_0)]^b & (\text{Coma Cluster}), \\ T_0 \frac{(r/r_{\text{cool}})^{a_{\text{cool}} + T_{\text{min}}/T_0}}{1 + (r/r_{\text{cool}})^{a_{\text{cool}}}} \frac{(r/r_t)^{-a}}{[1 + (r/r_t)^b]^{c/b}} & (\text{Perseus Cluster}). \end{cases} \quad (\text{A3})$$

In the appendix the temperature of gas is denoted by $T_{\text{gas}}(r)$ instead of $T(r)$, following the previous works (e.g., [35]). The fitting functions in Eq. (A3) are from Refs. [46] and [47] for the Coma Cluster and the Perseus Cluster, respectively, and the parameters are listed in Table VI and Table VII.

For the matter distribution, we assume the Navarro–Frenk–White (NFW) profile, Eq. (19), and the integrated mass within the radius r is given by

$$M(< r) = 4\pi \int_0^r dr r^2 \rho_{\text{NFW}}(r) = 4\pi \rho_s r_s^3 \left[\ln(1 + r/r_s) - \frac{r/r_s}{1 + r/r_s} \right], \quad (\text{A4})$$

which gives the gravitational potential by solving

$$\frac{d\psi(r)}{dr} = \frac{GM(< r)}{r^2}. \quad (\text{A5})$$

As described in Sec. III, we introduce the concentration parameter c and the virial mass M_{vir} instead of ρ_s and r_s . Here we follow the definition $M_{\text{vir}} = M(< r_{\text{vir}}) = 4\pi r_{\text{vir}}^3 \Delta_c \rho_c / 3$, where ρ_c is the critical density, and we adopt $\Delta_c = 100$, determined by the spherical collapse model [49].

For the demonstration in Sec. V, we simply adopt the fitted parameters obtained in previous works for the parameters in Eqs. (A2), (A3), and (19). The numerical values of the parameters are listed in Tables VI and VII for the Coma Cluster and the Perseus Cluster, respectively. The panels in Figs. 7 and 8 show the three dimensional profile of the temperature $T_{\text{gas}}(r)$, the gas mass density $\rho_{\text{gas}}(r)$, the variance of the random velocity $\sigma_{\text{rnd}}^2(r)$, the fraction of the nonthermal pressure to the total pressure $P_{\text{non-thermal}}(r)/P_{\text{total}}(r)$, the integrated mass $M(<r)$, and the gravitational potential $|\psi(r)|$.

TABLE VI: Fitted parameters for the Coma Cluster given in the previous works. Listed are the gas number density profile, Eq. (A2) (left table), the gas temperature profile, Eq. (A3) (middle table), in Ref. [35], and the NFW profile, Eq. (19) (right table), in Ref. [50].

n_{gas}	Terukina et al. [35]	T_{gas}	Terukina et al. [35]	ρ_{NFW}	Okabe et al. [50]
n_0	—	T_0	8.6 keV	M_{vir}	$8.95 \times 10^{14} h^{-1} M_{\odot}$
r_c	0.34 Mpc	A	0.082	c	3.5
β	0.67	r_0	3.9 Mpc		
		b	5.3		

TABLE VII: Fitted parameter values for the Perseus Cluster given in previous works. Listed are the intracluster gas number density profile, Eq. (A2) (left table), the gas temperature profile, Eq. (A3) (middle table), in Ref. [48], and the NFW profile, Eq. (19) (right table), in Ref. [51].

n_{gas}	Urban et al. [48]	T_{gas}	Urban et al. [48]	ρ_{NFW}	Simionescu et al. [51]
n_0	—	T_0	4.06 keV	M_{vir}	$8.05 \times 10^{14} M_{\odot}$
r_c	0.285 Mpc	T_{min}	2.92 keV	c	6.6
β	0.71	r_{cool}	0.29 Mpc		
		a_{cool}	6.72		
		r_t	1.6 Mpc		
		a	0.33		
		b	16.24		
		c	2.36		

- [1] N. Bartolo et al., Phys. Dark Univ. **13** (2016) 30
- [2] A. Raccanelli, D. Bertacca, D. Jeong, M. C. Neyrinck, A. S. Szalay, arXiv:1602.03186
- [3] A. Raccanelli, F. Montanari, D. Bertacca, O. Dore, R. Durrer, J. Cosmol. Astropart. Phys. 05(2016)009
- [4] D. Bertacca et al., arXiv:1705.09306
- [5] J. Yoo, Class. Quant. Grav. **31** (2014) 234001
- [6] J. Yoo, A. L. Fitzpatrick, M. Zalarriaga, Phys. Rev. D **80** 083514 (2009)
- [7] S. Alam, et al., Mon. Not. R. Astron. Soc. **470** 2822 (2017)
- [8] H. Zhu, et al., Mon. Not. R. Astron. Soc. **471** 2345 (2017)
- [9] R. Wojtak, S. H. Hansen, J. Hjorth, Nature **477** 567 (2011)
- [10] H. Zhao, J. A. Peacock, B. Li, Phys. Rev. D **88** 043013 (2013)
- [11] N. Kaiser, Mon. Not. R. Astron. Soc. **435** 1278 (2013)
- [12] P. Jimeno, T. Broadhurst, J. Coupon, K Umetsu, R. Lazkov, Mon. Not. R. Astron. Soc. **448** 199 (2015)
- [13] Y.-C. Cai, N. Kaiser, S. Cole, C. Frenk, Mon. Not. R. Astron. Soc. **468** 1981 (2016)
- [14] Hitomi Collaboration, Nature **535** 117 (2016), arXiv:1607.04487
- [15] S. Dodelson, *Modern Cosmology* (Academic Press, 2003)
- [16] M. White, Mon. Not. R. Astron. Soc. **321** 1 (2001)
- [17] U. Seljak, Mon. Not. R. Astron. Soc. **325** 1359 (2001)

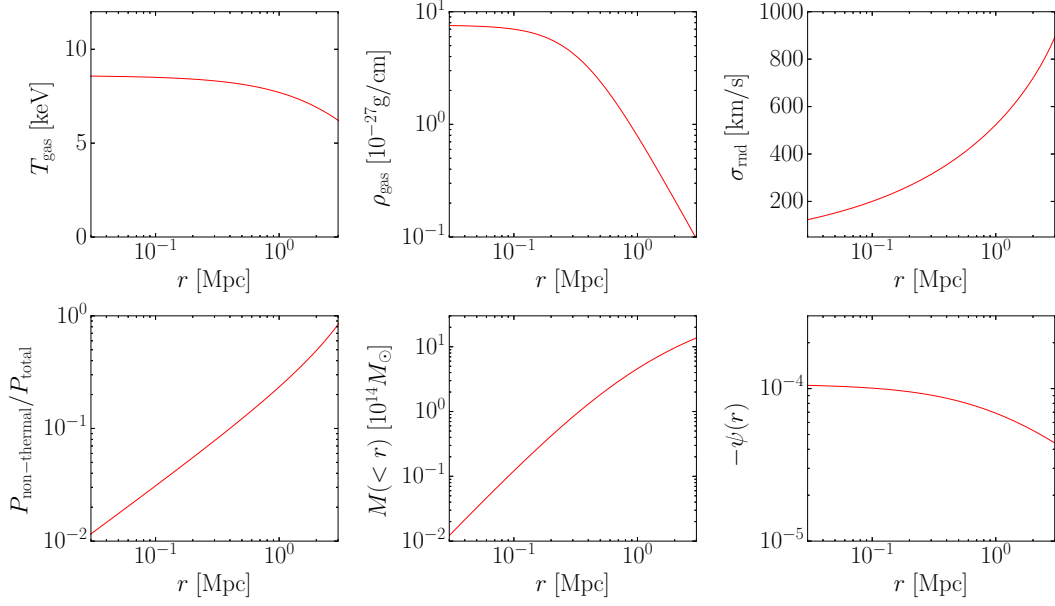


FIG. 7: Three-dimensional profiles of the various quantities for the Coma Cluster used for Fig. 3.

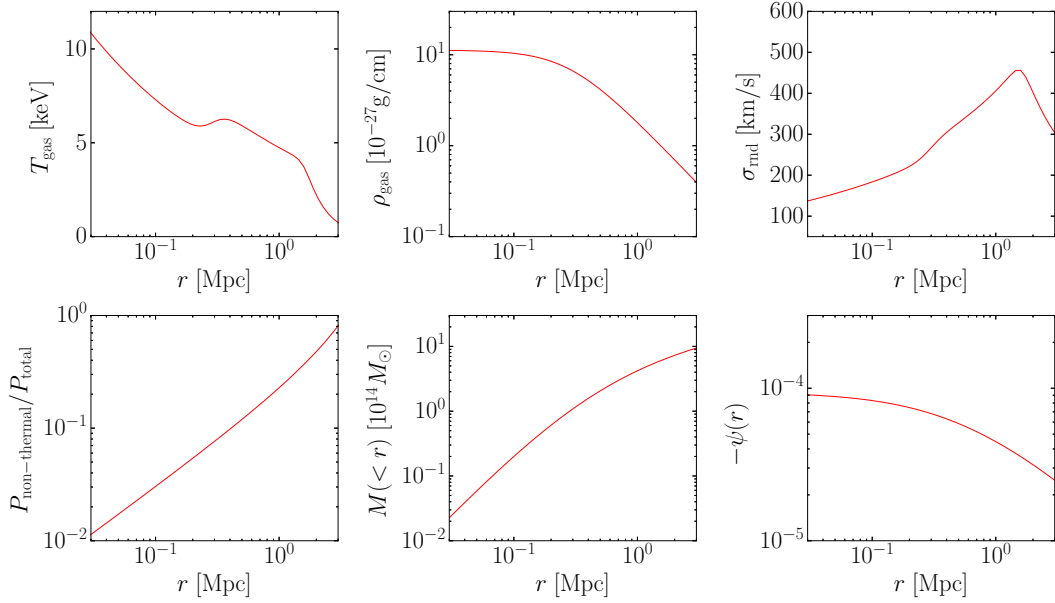


FIG. 8: Same as Fig. 7 but for the Perseus Cluster used for Fig. 4.

- [18] A. Cooray, R. Sheth, Phys. Rep. **372** 1 (2002)
- [19] Z. Zheng et al., Astrophys. J. **633** 791 (2005)
- [20] B. A. Reid, D. N. Spergel, Astrophys. J. **698** 143 (2009)
- [21] C. Hikage, K. Yamamoto, J. Cosmol. Astropart. Phys. 08(2013)019
- [22] C. Hikage, K. Yamamoto, Mon. Not. R. Astron. Soc. Lett. **455** L77 (2015)
- [23] C. Hikage, R. Mandelbaum, M. Takada, D. N. Spergel, Mon. Not. R. Astron. Soc. **435** 2345 (2013)
- [24] T. Kanamaru, C. Hikage, G. Huetsi, A. Terukina, K. Yamamoto, Phys. Rev. D **92** 023523 (2015)
- [25] J. F. Navarro, C. S. Frenk, S. D. White, Astrophys. J. **490** 493 (1997)

- [26] J. K. Parejko et al., *Mon. Not. Roy. Astron. Soc.* **429** 98 (2013)
- [27] M. Manera et al., *Mon. Not. Roy. Astron. Soc.* **428** 1036 (2013)
- [28] R. K. Sheth, G. Tormen, *Mon. Not. R. Astron. Soc.* **308** 119 (1999)
- [29] R. K. Sheth, G. Tormen, *Mon. Not. Roy. Astron. Soc.* **329** 16 (2002)
- [30] H. Parkinson, S. Cole J. Helly, *Mon. Not. Roy. Astron. Soc.* **383** 557 (2008)
- [31] T. Broadhurst, E. Scannapieco, *Astrophys. J.* **533** L93 (2000)
- [32] K. Yamamoto, H. Sato, N. Sugiyama, *Phys. Rev. D* **56** 7566 (1997)
- [33] N. Battaglia et al., *Astrophys. J.* **758** 74 (2012)
- [34] L. D. Shaw et al., *Astrophys. J.* **725** 1452 (2010)
- [35] A. Terukina, L. Lombriser, K. Yamamoto, D. Bacon, K. Koyama, R. C. Nichol, *J. Cosmol. Astropart. Phys.* 04(2014)013
- [36] A. Terukina, K. Yamamoto, N. Okabe, K. Matsushita, T. Sasaki, *J. Cosmol. Astropart. Phys.* 10(2015)064
- [37] X. Shi, E. Komatsu, K. Nelson, D. Nagai, *Mon. Not. R. Astron. Soc.* **448** 1020 (2015)
- [38] N. Hamaus, P. M. Sutter, B. D. Wandelt, *Phys. Rev. Lett.* **112** 251302 (2014)
- [39] Q. Mao et al., *Astrophys. J.* **835** 160 (2017).
- [40] D. Micheletti et al., *Astron. Astrophys.* **570** A106 (2014)
- [41] Y.-C. Cai, N. Padilla, B. Li, *Mon. Not. R. Astron. Soc.* **451** 1036 (2015)
- [42] A. J. Hawken et al., *Astronomy and Astrophysics*, **607** A54 (2017)
- [43] N. Hamaus et al., *Journal of Cosmology and Astroparticle Physics*, 07(2017)014
- [44] I. Achitouv, arXiv:1707.08121
- [45] A. Cavaliere, R. Fusco-Femiano, *Astron. Astrophys.* **70** 677 (1978)
- [46] J. O. Burns, S. W. Skillman, B. W. O'Shea, *Astrophys. J.* **721** 1105 (2010)
- [47] A. Vikhlinin, A. Kravtsov, W. Forman et al., *Astrophys. J.* **640** 691 (2006)
- [48] O. Urban, A. Simionescu, N. Werner et al., arXiv:1307.3592
- [49] T. T. Nakamura, Y. Suto, *Prog. Theor. Phys.* **97** 49 (1997)
- [50] N. Okabe, Y. Okura, T. Futamase, *Astrophys. J.* **713** 291 (2010)
- [51] A. Simionescu et al., *Science* **331** 25 (2011)